Proceedings of the
Annual Stability Conference
Structural Stability Research Council
Atlanta, Georgia, April 21-24, 2026

High-strength cold-formed steel columns prone to local and local-distortional interactive buckling

André D. Martins[1], João A. Lazzari[2], Rodrigo Gonçalves[3], Nuno Peres[4]

Abstract

This study presents an experimental investigation concerning the structural behavior of high-strength cold-formed steel (CFS) columns prone to local and/or distortional buckling. The experimental campaign, carried out at the University of Lisbon, involved testing channel and lipped channel columns, brake-pressed from high-strength steel grade S700 (proof strength exceeding 800 MPa), supplied by SSAB (Sweden). The column geometries were carefully selected to enable the testing of short and short-to-intermediate fixed-ended columns subjected to two instability phenomena: (i) web-triggered local buckling, and (ii) local-distortional mode interaction. Prior to the structural tests, (i) material properties were determined through standardized tensile coupon tests in accordance with EN ISO 6892-1, including an assessment of their variability, and (ii) initial geometric imperfections were quantified based on high-resolution measurements obtained using a handheld 3D laser scanner, combined with the development of a novel approach to characterize these imperfections. The structural tests were performed using a 600 kN Universal Testing Machine under displacement-control, with two complementary data acquisition systems: (i) Linear Variable Differential Transformers (LVDTs), and (ii) a Digital Image Correlation (DIC) system.

1. Introduction

High-strength cold-formed steel (HSCFS) profiles have gained increasing prominence in the field of steel construction due to their high structural efficiency and significant potential for weight optimization. The combination of cold-forming processes with high yield stress steels enables the production of high strength structural elements, while maintaining low manufacturing costs and reducing material consumption. High-strength steels (HSS) are characterized by a proof stress between 460 MPa and 690 MPa (Wang *et al*. 2021). However, the present paper concerns advanced steel grades, which exhibit specific features that render the development of efficient/reliable design rules rather challenging: (i) the constitutive relations are considerably more complex, (ii) the members become markedly more susceptible to complex coupled buckling phenomena (Camotim *et al*. 2020a,b), and (iii) all ultimate limit states require reassessment since the significantly higher proof and ultimate strengths (albeit Young's

[1] Assistant Researcher, CERIS, Instituto Superior Técnico, Universidade de Lisboa, <andrerdmartins@tecnico.ulisboa.pt>
[2] PhD student, CERIS, Instituto Superior Técnico, Universidade de Lisboa, <joao.lazzari@tecnico.ulisboa.pt>
[3] Full Professor, CERIS, Faculdade de Ciências e Tecnologia, Universidade Nova de Lisboa, <rodrigo.goncalves@fct.unl.pt>
[4] Assistant Researcher, Laboratório Nacional de Engenharia Civil (LNEC), Portugal, <nperes@lnec.pt >

modulus is similar) cannot simply be accommodated by adjusting existing design rules for CFS members through new/updated resistance (or partial safety) factors. These issues must be addressed before HSCFS members can be efficiently designed and become economically attractive.

The behavior of these profiles is strongly governed by instability phenomena such as local (L), distortional (D) and global (G) buckling, together with coupled buckling phenomena (L-G, L-D, D-G and L-D-G interaction), the understanding of which is essential to ensure structural safety and an appropriate structural performance. Consequently, the investigation of the mechanical and structural response of HSCFS members constitutes a topic of high scientific interest and relevance in Structural Engineering, particularly given that these steel grades cannot yet be readily applied in the construction industry, as currently no structural design code formally covers them. This present investigation focuses exclusively on HSCFS columns (uniform compression) and belongs to the ongoing research project NXGEN-CFSS: "Towards the Next Generation of Cold-Formed Steel Structures: Advanced High Strength Steels", motivated by the lack of knowledge on the structural behavior of HSCFS members and the absence of appropriate design rules.

2. Brief state-of-the-art review

2.1 Material behavior

Gardner & Yun (2018) proposed a comprehensive constitutive model for CFS based on more than 700 experimental stress-strain curves covering a wide range of steel grades, thicknesses and cross-section shapes. A two-stage Ramberg-Osgood (R-O) formulation, adapted from Mirambell & Real (2000) stainless steel investigation, was used to capture the rounded stress-strain response characteristic of cold-formed carbon steels. Predictive expressions were provided for the key material parameters, including (conventional) yield and ultimate strengths, strain-hardening exponents and ultimate strain, with separate treatment of flat and corner regions to account for cold-forming effects. The model showed very good agreement with test data and is robust across different levels of material input data, from basic yield strength data to full (complete) material property sets, making it suitable for numerical simulations and design applications.

Xia *et al*. (2021) conducted a material characterization study on advanced high-strength steels (AHSS), including 43 tensile tests (ASTM E8/E8M-16, 2016) and the development of a new stress-strain model for five AHSS grades (DP-340, DP-580, DP-700, MS-1030 and MS-1200) and one conventional high-strength low-alloy (HSLA-700). The proposed model, an updated two-stage R-O formulation with an additional linear stage, depending on 5 material properties and 2 non-linear parameters, showed excellent agreement with test data. Predictive equations for material parameters and strain-hardening exponents were also provided. Unlike the previous model, the proof stress is not necessarily defined at 0.2% proof stress and varies with each AHSS.

2.2 Structural behavior

The analysis of the state-of-the-art involving HSS in Civil Engineering reveals that applications are very scarce and recent. During his PhD, Ding (2022) investigated the behavior of AHSS structural components, including connections, beams, and columns, through extensive experimental and numerical studies. Ding *et al*. (2022) conducted 54 four-point bending tests, 156 column tests, and a series of bolted lap-shear tests on dual-phase (DP) and martensitic (MS) steels with several steel grades (DP340, 500, 700 and MS1030, 1200). Bolted lap shear connection tests were performed on specimens prone to bearing, tilting/bearing, net-tension and end tear-out failure modes. Reduced ductility was shown to decrease connection strength, with AISI provisions generally providing conservative but sometimes

inconsistent strength predictions. Column tests on lipped channels and sigma-sections, tested under "bare-end" boundary conditions, revealed local, distortional, L-D and L-D-G interactive failures, with DSM predictions proving unreliable for slender, high strength sections. These findings highlight the need to adjust current design methodologies to account for the unique characteristics of AHSS.

The AHSS beam tests reported by Ding *et al*. (2026) revealed that specimens made from higher yield strength (≥700 MPa) frequently exhibited L-D interaction, which negatively affected their ultimate strength. A small number of specimens failed in pure local or distortional modes. The current DSM design equations in AISI S100 (2022) and AS/NZS 4600 (2018) were found to be unconservative, particularly for high-strength materials. To improve prediction accuracy, the study explored modified DSM approaches, including reducing the yield stress to reflect limited ductility and explicitly incorporating L-D buckling as a limit state, following the NLD approach proposed by Martins *et al*. (2017). These modifications resulted in more reliable strength predictions. Overall, the results highlighted the need to revise existing DSM design provisions for AHSS in CFS members, especially at high slenderness values where L-D interactions are more pronounced.

Akchurin *et al*. (2025) investigated the axial compressive behavior of CFS stiffened channel sections, roll-formed from 1.9-mm HSLA steel with a nominal yield strength of 690 MPa. Seventeen columns of three lengths (305, 610 and 1220 mm) were tested under bare steel-to-steel end conditions using a Universal Testing Machine. Combined with elastic buckling analysis and detailed imperfection measurements, the study identified two distortional buckling modes and their interaction as governing failures. The results showed good agreement with DSM predictions, particularly considering simply supported conditions.

Recently, Ma *et al*. (2026) investigated high-strength CFS built-up I-section profiles subjected to combined compression and minor-axis bending. Ten back-to-back screw-connected channel sections, press-braked from 2.9-mm S700 steel, were tested and all failed by local buckling. A validated shell finite element model was used to perform a parametric study assessing the accuracy of the bending-axial interaction curves of Eurocode 3-1-3 (2024), AISI S100 (2022) (via both the Effective Width Method and DSM), and a modified AISI formulation. All design methods were found to be conservative, though to varying degrees.

3. Experimental campaign: material characterization tests

3.1 Material description

The material considered in this study is a high-strength steel grade S700 Strenx® 700 CR, manufactured by SSAB (Sweden). This cold-rolled structural steel, according to the producer's technical documentation, exhibits: (i) a minimum yield strength of 700 MPa (0.2% proof stress), (ii) an ultimate tensile strength in the range 1000-1200 MPa, and (iii) a minimum fracture elongation of 7 % measured over an 80 mm gauge length. To characterize both the material and evaluate the variability, 78 test coupons were extracted along the rolling direction. Additional 5 specimens were extracted in each of the transverse and ± 45° orientations, to evaluate the isotropy of the material, yielding a total of 93 samples. All specimens were machined through Computerized Numerical Controller (CNC) cutting to avoid property alterations associated with thermal cutting methods such as laser processing.

3.2 Test procedures and instrumentation

The material characterization tests were conducted at the Laboratory of Structures and Strength of Materials (LERM), within the Department of Civil Engineering at Instituto Superior Técnico (IST).

Material testing was carried out on an Instron 5989 Universal Testing Machine (UTM) with a 600 kN load capacity. A video extensometer (VE) system was employed to record the strains at selected reference points marked on the test specimens. A FLIR BFS-U3-51S5M-C camera (5 MP, 2448 × 2048) equipped with a Fujinon HF25SA-1 lens (25 mm focal length, adjustable aperture F/1.4-F/22) recorded the displacement of marked points on the specimens. The camera was mounted on a tripod at roughly 500 mm from the samples. Fig. 1(a) outlines the test configuration, while Fig. 1(b) provides a closer view of the lens, the UTM, and a specimen under testing. Maximum load values were taken from the UTM, and all other measurements from the VE.

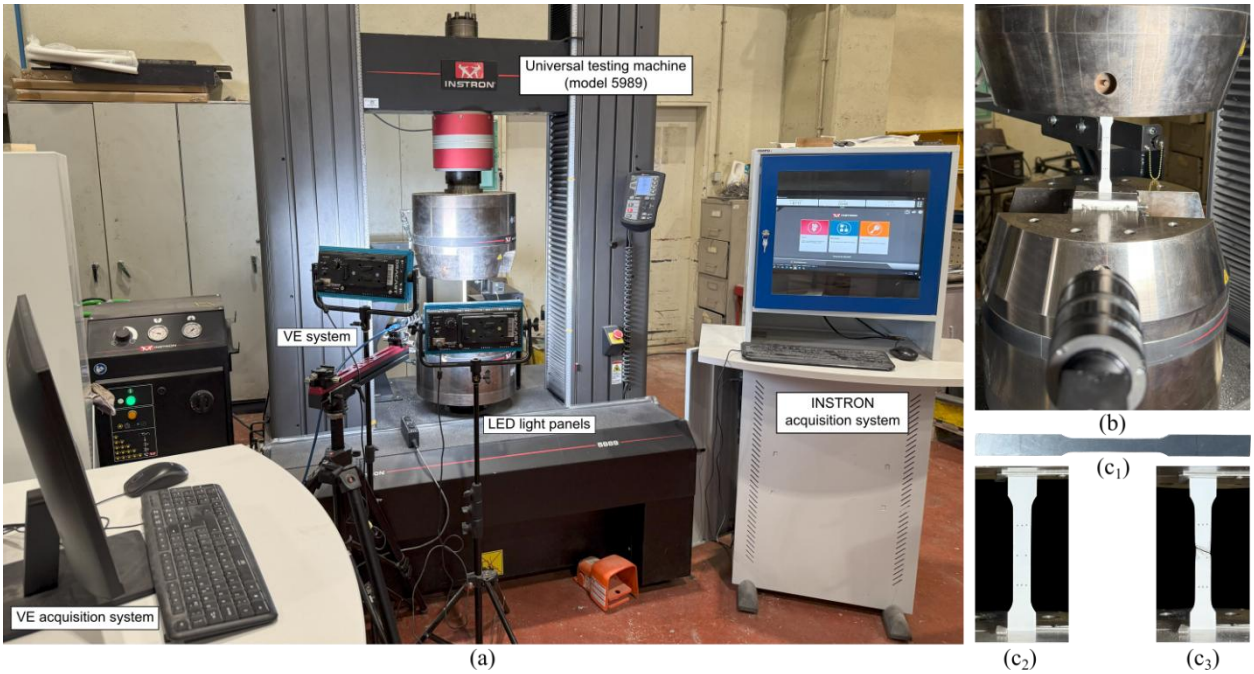

Figure 1: Tensile test setup (a) general view, (b) detailed view, and representative coupon (c_1) after machining, (c_2) prior (painted and with reference dots) and (c_3) after the mechanical test.

The tensile tests followed EN ISO 6892-1 (2019) and the coupon geometry complied with Annex B (sheet thicknesses between 0.1 and 3 mm), using type 2 specimens: 75 mm parallel length, 12.5 mm width, 50 mm original gauge length (L_c) and 20 mm transition radius – the geometry is shown in Fig. 2. Before testing, each specimen (Fig. 1(c_1)) was sprayed with two white paint layers, after which nine black reference marks were added manually (Fig. 2). These points enabled the measurement of longitudinal and transverse strains in six regions (3 in each direction). The longitudinal gauge length (L_e) followed Clause 8.3 of the standard, with $L_e = L_0 = 50$ mm. Tensile tests followed Method A2 of the standard, which requires controlling the estimated strain rate over the parallel length ($\dot{e}_{L_c}$). Thus, testing was performed under crosshead displacement control using $v_c = L_c \cdot \dot{e}_{L_c}$. A constant strain rate was applied throughout the entire test corresponding to a crosshead speed of $50 \times 0.00025 = 0.75$ mm/min, and the total test duration was roughly 10-11 minutes. The test campaign aimed to quantify the variability of six material properties: elastic modulus (E), total extension at maximum force (A_{gt}), tensile strength (σ_u), 0.2% proof stress ($\sigma_{p0.2}$), total elongation at fracture (A_t), and Poisson's ratio (ν). The elastic modulus was evaluated according to Annex G of the standard, using a least-squares procedure applied between lower and upper stress limits of approximately $0.10\sigma_{p0.2}$ and $0.40\sigma_{p0.2}$.

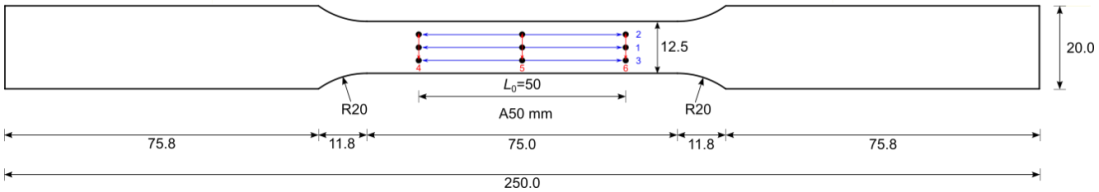

Figure 2: Geometry of the tensile coupon according to EN ISO 6892-1 (2019): test piece type 2 (dimensions in mm)

3.3 Results and discussion

Figure 3 presents the longitudinal tensile test results (the transverse and ±45° directions test results are omitted). All engineering stress (σ_x)-strain (ε_x) curves show an initial elastic region, followed by a smooth nonlinear transition without a distinct yield point, then a plastic plateau and a final drop in engineering stress until failure. Overall, the σ_x-ε_x responses are qualitatively similar across orientations, with the transverse specimens displaying a lower ductility. The variability in elastic modulus E is small, whereas the scatter in A_t is considerably larger.

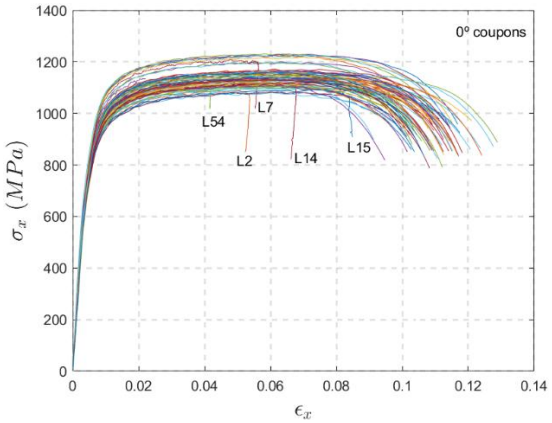

Figure 3: Engineering σ_x vs ε_x curves for the longitudinal coupons.

Table 1 presents the main descriptive statistics for the longitudinal tests, namely mean ($\hat{\mu}$), standard deviation ($\hat{\sigma}$), coefficient of variation (CoV), and minimum/maximum values, for E, σ_u, $\sigma_{0.2p}$, A_{gt}, A_t and ν. The measured properties agree with the manufacturer's specifications: minimum proof stress of 700 MPa, ultimate tensile strength between 1000-1200 MPa, and minimum elongation of 7.0 %. The results show low variability in E, σ_u and $\sigma_{0.2p}$ (CoV≤ 5%), while A_{gt}, A_t and ν exhibit slightly higher dispersion, though generally below 10%. The higher scatter in ν is attributed to lower precision when measuring small deformations and using shorter gauge lengths, resulting in higher signal noise in the transverse strain measurements and, consequently, in the determination of ν.

Table 1: Summary of longitudinal test results: mean value ($\hat{\mu}$), standard deviation ($\hat{\sigma}$), CoV, and number of valid tests.

Material property	$\hat{\mu}$	$\hat{\sigma}$	CoV (%)	min	max	Nº valid tests
E (GPa)	194.78	9.77	5.0	168.85	224.12	77
σ_u (MPa)	1152.18	35.73	3.1	1087.58	1242.53	76
$\sigma_{0.2p}$ (MPa)	867.67	33.32	3.8	810.06	958.43	77
A_{gt} (%)	6.287	0.690	11.0	4.523	8.036	73
A_t (%)	10.999	0.775	7.0	9.106	12.880	67
ν (-)	0.311	0.029	9.3	0.261	0.393	75

It is worth nothing that some results were excluded due to equipment or measurement issues: (i) one test was interrupted by a UTM malfunction (specimen L-54), precluding the determination of σ_u, A_{gt} and A_t,

(ii) four tests had incomplete VE recordings (specimens L-21, L-23, L-32 and L-44), which prevented the determination of A_{gt} and/or A_t, and (iii) in five tests fractures occurred outside the gauge length (specimens L-2, L-7, L-14, L-53 and L-61), precluding the determination of A_t.

3.4 Constitutive model

This section aims to select a suitable constitutive model for Strenx® 700 CR steel. Based on the σ_x-ε_x curves in Fig. 3, two models are selected as candidates for representing the material response up to the ultimate stress. The first candidate is the two-stage Ramberg-Osgood model (RO_{2s}), originally proposed by Mirambell & Real (2000) for stainless steels, which effectively captures the rounded stress–strain behavior typical of high-strength steels. It is defined as follows:

$$\varepsilon = \begin{cases} \frac{\sigma}{E} + 0.002\left(\frac{\sigma}{\sigma_{0.2}}\right)^n, \ \sigma \leq \sigma_{0.2} \\ \frac{\sigma-\sigma_{0.2}}{E_{0.2}} + \left(\varepsilon_u - \varepsilon_{0.2} - \frac{\sigma_u-\sigma_{0.2}}{E_{0.2}}\right).\left(\frac{\sigma-\sigma_{0.2}}{\sigma_u-\sigma_{0.2}}\right)^m + \varepsilon_{0.2}, \ \ \sigma_{0.2} < \sigma \leq \sigma_u \end{cases} \quad (1)$$

with $E_{0.2} = \frac{E}{1+0.002 \cdot n \cdot \frac{E}{\sigma_{0.2}}}$, and where n is the 1st strain hardening exponent, m is the 2nd strain hardening exponent, $\sigma_{0.2}$ is the conventional yield strength (0.2% proof stress), E Young's modulus, σ_u is the ultimate tensile strength, ε_u is the strain at σ_u, and $E_{0.2}$ is the tangent modulus at the 0.2% proof stress.

The second model, proposed by Xia *et al.* (2021), was developed from material tests on advanced high-strength steels (AHSS). It is an enhanced two-stage Ramberg-Osgood formulation that includes an additional linear segment (denoted RO_{u2s+ls}). The constitutive model is given by

$$\varepsilon = \begin{cases} \frac{\sigma}{E} + p\left(\frac{\sigma}{\sigma_p}\right)^n, \ \sigma \leq \sigma_p \\ \frac{\sigma-\sigma_p}{E_p} + \left(\varepsilon_{eu} - \varepsilon_p - \frac{\sigma_{eu}-\sigma_p}{E_p}\right).\left(\frac{\sigma-\sigma_p}{\sigma_{eu}-\sigma_p}\right)^m + \varepsilon_p, \ \ \sigma_p < \sigma \leq \sigma_{eu} \\ \varepsilon_{eu} + (\sigma - \sigma_{eu}).\frac{\varepsilon_u-\varepsilon_{eu}}{\sigma_u-\sigma_{eu}}, \sigma_{eu} < \sigma \leq \sigma_u \end{cases} \quad (2)$$

with (i) $E_p = \frac{E}{1+p \cdot n \cdot \frac{E}{\sigma_p}}$, (ii) $\varepsilon_p = \frac{\sigma_p}{E} + p$, and (iii) $\sigma_{eu} = 0.99\sigma_u$, and where ε_p and σ_p are the strain and stress of p offset (with a plastic strain of p), E_p is the tangent modulus at σ_p, ε_{eu} and σ_{eu} are the strain and stress of the equivalent ultimate point, respectively – the equivalent point is defined as the point with a stress equal to 99% of the ultimate strength at strain hardening stage. This model thus depends on six material properties (E, σ_p, ε_{eu}, σ_{eu}, ε_u, σ_u) and two nonlinear parameters (n and m). Unlike the previous model, the proof stress is not fixed at 0.2% and instead varies with the specific HSS grade.

The following MATLAB-based procedure was implemented to identify the most suitable constitutive model for Strenx® 700 CR steel:

1. The VE data were smoothed using a LOWESS (LOcally WEighted Scatterplot Smoothing) filter to reduce measurement noise.
2. A set of uniformly spaced points (N_p) along the curve (arclength) was determined. For this purpose, an auxiliary curve was first constructed through the linear interpolation of the experimental data points

while accounting for the different ranges of the *x*- and *y*-axes, *i.e.*, a scale factor of σ_u/ε_u was applied to the *x*-values (ε values). A total of N_p=100 points was considered adequate for this procedure.

3. A classical least square optimization problem with constrained admissible domains was then solved using two approaches: a classical interior-point algorithm and a genetic algorithm (GA).

The optimization results showed that the RO_{2s} model did not provide satisfactory agreement with the experimental results in the transition region between the two stages, whereas the RO_{u2s+ls} model achieved excellent agreement across the full range, with an average coefficient of determination (R^2 value) of 0.9908. Moreover, the GA solutions were consistently, though marginally, better than those obtained with a classical optimization method.

3.5 Statistical analysis

Identifying suitable probability distributions for each material parameter is essential for quantifying uncertainty and deriving statistical descriptors such as means, CoVs and characteristic values. In this study, the distribution parameters were estimated using the popular Maximum Likelihood Estimation method. Goodness-of-fit was evaluated using both the Chi-square and Anderson-Darling (A-D) tests. The first test depends on data binning and reflects overall agreement, whereas the latter is bin-independent and more sensitive to tail behavior, an important aspect in structural reliability. This analysis extends the guidance provided in the Probabilistic Model Code (2001), which is limited to steels with yield strengths up to 380 MPa.

Figure 4 presents normalized histograms and fitted probability density functions (PDFs) for the 6 material properties obtained from the longitudinal tensile tests (E, σ_u, $\sigma_{p0.2}$, A_{gt}, A_t, ν). Seven candidate PDFs were examined: Lognormal, Normal, Gamma, Weibull (extreme type III distribution), Gumbel (extreme type I distribution), Nakagami and Logistic. Table 2 reports the inference analysis and Chi-square goodness-of-fit results for the 6 random variables (E, σ_u, $\sigma_{0.2p}$, A_{gt}, A_t, ν). For each variable, the table lists the selected probabilistic model(s), mean, standard deviation, CoV and characteristic value. Characteristic values correspond to the 5% fractile of the fitted distribution, following Clause 6.2 of EN 1990 (2023). When two distributions are shown, the first is the best-fitting model (lowest test statistic), and the second is the Lognormal distribution, included for reference given its common use in modelling material properties (*e.g.*, Probabilistic Model Code, 2001). Table 3 provides the Chi-square results at a 5% significance level, and it can be concluded that Lognormal, Gamma, Nakagami and Logistic distributions adequately model all variables, while the Normal distribution fits 5 of the 6 material properties. In contrast, the Gumbel and Weibull distributions show poorer overall performance, and the Lognormal (Logistic) distribution provided the best fit for σ_u, A_{gt}, and ν (E, $\sigma_{0.2p}$ and A_t).

Table 2: Probabilistic models adopted for each mechanical property according to the Chi-square goodness-of-fit tests (α=0.05).

Material property	Probabilistic model	Mean	Standard deviation	CoV (%)	Characteristic value
E (GPa)	Logistic	194.959	9.698	4.97	179.216
	Normal	194.784	9.772	5.02	178.711
σ_u (MPa)	Lognormal	1152.175	35.380	3.07	1094.922
$\sigma_{0.2p}$ (MPa)	Logistic	865.341	34.239	3.96	809.760
	Lognormal	867.670	32.986	3.80	814.505
A_{gt} (%)	Lognormal	6.288	0.700	11.13	5.207
A_t (%)	Logistic	10.972	0.809	7.37	9.659
	Lognormal	10.999	0.773	7.03	9.775
ν (-)	Lognormal	0.311	0.028	9.05	0.267

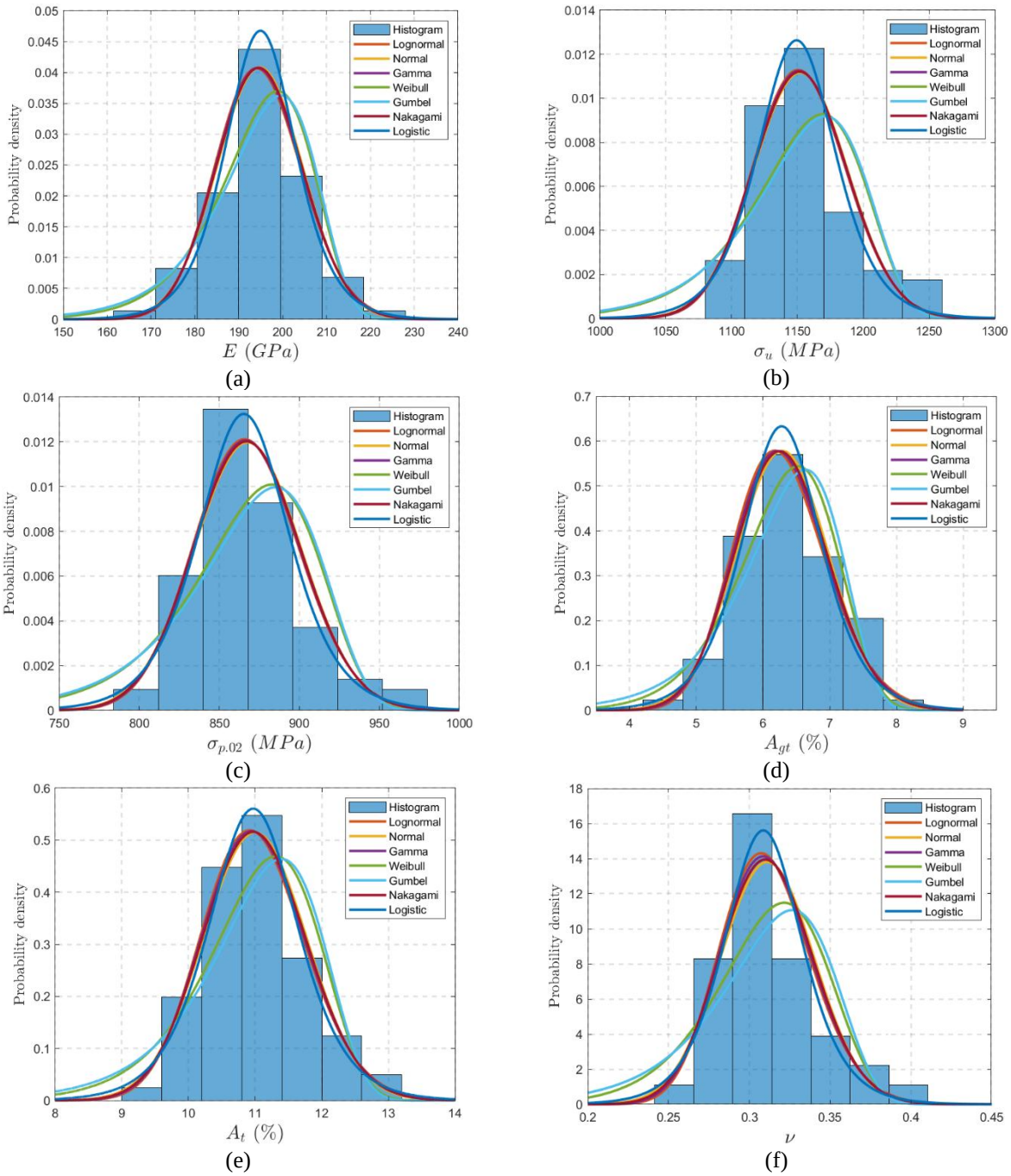

Figure 4: Histograms and fitted probability density functions of (a) E, (b) σ_u, (c) $\sigma_{0.2p}$, (d) A_{gt}, (e) A_t, and (f) ν (longitudinal coupons).

Table 3: Summary of the Chi-square goodness-of-fit tests (α=0.05).

Material property	Lognormal	Normal	Gamma	Weibull	Gumbel	Nakagami	Logistic
E	✓	✓	✓	✓	✓	✓	✓
σ_u	✓	✓	✓	×	×	✓	✓
$\sigma_{0.2p}$	✓	✓	✓	×	×	✓	✓
A_{gt}	✓	✓	✓	✓	×	✓	✓
A_t	✓	✓	✓	×	×	✓	✓
ν	✓	×	✓	×	×	✓	✓

✓: H_0 not rejected; ×: H_0 not rejected.

Tables 4 and 5 summarize the A-D goodness-of-fit results and closely resemble those related to the Chi-square outcomes in Tables 2 and 3. The main differences are: (i) Table 4 reports only the best-fitting distribution (lowest test statistic), (ii) less commonly used distributions (Nakagami and Logistic) were omitted, and (iii) a 5% significance level was generally used, except for σ_u where it was reduced to avoid rejecting all candidate distributions. Comparing Tables 2 and 4 shows good agreement between the two test methods, with the main difference occurring for A_{gt}, for which the Gamma distribution is now the most suitable model. Since the fitted distributions capture accurately the experimental observations, the descriptive statistics derived from them closely match the directly observed values reported in Table 1.

Table 4: Probabilistic models adopted for each mechanical property according to the A-D goodness-of-fit tests.

Material property	Probabilistic model	Mean	Standard deviation	CoV (%)	Characteristic value
E (GPa)	Normal	194.784	9.772	5.02	178.711
σ_u (MPa)	Lognormal	1152.175	35.380	3.07	1094.922
$\sigma_{0.2p}$ (MPa)	Lognormal	867.670	32.986	3.80	814.505
A_{gt} (%)	Gamma	6.287	0.694	11.03	5.192
A_t (%)	Lognormal	10.999	0.773	7.03	9.775
ν (-)	Lognormal	0.311	0.028	9.05	0.267

Table 5: Summary of the Summary of the Anderson-Darling goodness-of-fit tests.

Material property	α	Lognormal	Normal	Gamma	Weibull	Gumbel
E	0.05	✓	✓	✓	×	×
σ_u	0.01	✓	×	✓	×	×
$\sigma_{0.2p}$	0.05	✓	×	✓	×	×
A_{gt}	0.05	✓	✓	✓	✓	×
A_t	0.05	✓	✓	✓	×	×
ν	0.05	✓	×	✓	×	×

✓: H_0 not rejected; ×: H_0 not rejected

4. Experimental campaign: structural tests

4.1 HSCFS column specimens

The CFS profiles were fabricated from the same high-strength steel used in the material characterization tests. Steel sheets with a thickness of 2 mm were press-braked to form several profiles with two distinct cross-section shapes for structural testing: channel (U) and lipped channel (C). Table 6 presents the nominal dimensions of the 10 profiles (6 lipped channels and 4 channels), obtained after press-braking, while the nomenclature of the cross-section dimensions is shown in Fig. 5. In this Table, L is column length, n_L is the critical local buckling half-wave number, $P_y=A\sigma_{0.2p}$ is the squash load, P_{crL} and $P_{crL,Exp}$ are the numerical and experimental critical local buckling loads, λ_L is the local slenderness, and $P_{U,Exp}$ the ultimate load.

Table 6: CFS profiles: nominal dimensions after press-braking of steel sheets, critical local buckling loads and ultimate loads.

Profile	h (mm)	b (mm)	c (mm)	r_i (mm)	t (mm)	L (mm)	P_{crL} (kN)	n_L	$P_{crL,Exp}$ (kN)	P_y (kN)	λ_L	$P_{U,Exp}$ (kN)	Failure mode
P1	115.64	59.18	21.00	6.95	2.00	500	165.61	5	171.36	451.1	1.65	284.98	Local
P2	106.74	51.31	21.00	6.95	2.00	500	179.22	5	174.58	408.4	1.51	288.52	Local
P3	106.00	74.28	21.07	6.95	2.00	500	202.85	5	216.43	486.9	1.55	267.93	Local
P4	97.65	54.20	21.00	6.95	2.00	800	205.45	10	206.63	402.7	1.40	260.71	Local
P5	137.25	94.90	20.80	6.95	2.00	600	149.07	5	158.86	611.4	2.03	260.46	Local
P6	121.46	59.00	21.00	6.95	2.00	800	151.21	8	150.29	460.5	1.75	255.85	L-D
P8	98.80	49.00	-	6.95	2.00	700	86.07	5	89.43	327.3	1.95	148.34	Local
P9	108.43	49.00	-	6.95	2.00	700	84.32	5	82.44	344.0	2.02	148.98	Local
P10	118.30	49.00	-	6.95	2.00	750	81.03	5	81.96	361.1	2.11	153.22	Local
P11	128.25	49.00	-	6.95	2.00	750	76.53	5	76.74	378.3	2.22	146.22	Local

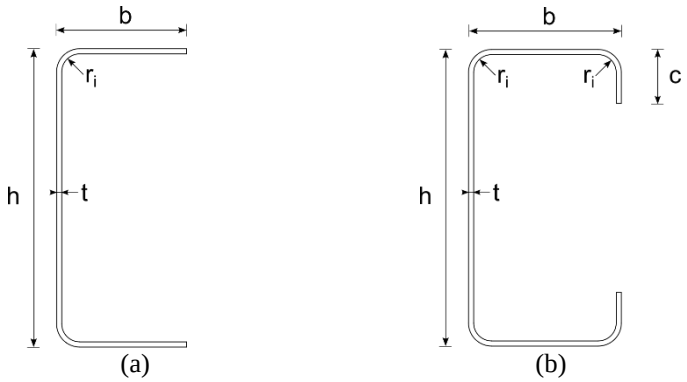

(a) (b)

Figure 5: Nomenclature of the (a) channel (U) and (b) lipped channel (C) columns.

4.2 Laser scanning

Prior to the structural tests, the 10 CFS profiles were scanned using a high-resolution handheld 3D laser scanner to determine the initial geometric imperfections (discussed in Section 4.3). During the digitalization of the CFS profiles, a high-resolution (0.05 mm) and high-accuracy (0.05 mm) Artec Spider II handheld 3D laser scanner was used. The measurement/digitalization process of the CFS profiles involved the following steps, with the setup illustrated in Fig. 6(a):

1. **Pre-digitization:** The profiles were coated with a matte white (non-glossy) spray to mitigate scanning issues associated with the reflective surface of the steel.
2. **Capture/Digitalization:** After connecting and calibrating the scanner using Artec Studio software, the laser scanner was used to capture the various walls of the profiles along their length by steadily moving the device around the object. Multiple scans were performed, and several reference markers were employed (omitted in the figure for clarity) to measured specific regions (*e.g.*, the lips of the C-sections).
3. **Processing:** The captured scans were aligned into a single coordinate system using the Artec Studio software. Subsequently, noise and/or small unwanted objects were then removed.
4. **Fusion/3D Mesh Generation:** After alignment, the scan data were merged to generate a 3D mesh.
5. **Post-processing:** Using Blender (Blender Foundation, 2026), the mesh was smoothed, the number of triangles reduced (if necessary), and the end plates and weld beads were removed. The cut regions were then adjusted to ensure compatibility. For illustrative purposes, Fig. 6(b) shows the scanned P11 profile, including a detailed view of a (raw) mesh region.

(a) (b)

Figure 6: (a) Experimental setup for laser scanning of CFS profiles, and (b) post-processed P11 scanned profile.

4.3 Initial geometrical imperfections

The initial geometric imperfections are quantified using point clouds obtained from the 3D scans of each profile. Generalized Beam Theory (GBT) is employed to identify the geometric imperfections through modal decomposition. A dedicated procedure was developed, comprising the following steps:

1. **Initial alignment of the scanned geometry:** Using Meshlab (Cignoni *et al.* 2008), the raw point cloud of each profile is aligned with a corresponding perfect 3D model using the built-in Iterative Closest Point (ICP) algorithm.
2. **Extraction of cross-section point clouds:** A custom Python script was developed to extract multiple cross-sectional point clouds at discrete locations along the profile length from the aligned 3D scan.
3. **GBT mode generation and normalization:** The GBT deformation modes are initially obtained using GBTUL (Bebiano *et al.* 2018), where the rounded corners of the cross-section are taken into account and approximated by a series of short straight segments. The procedure proposed in Gonçalves and Camotim (2016) is then applied to correct the local-plate modes. The (i) rigid body (excluding axial extension), (ii) distortional and (iii) local-plate modes are finally normalized such that the maximum transverse displacement of each mode is equal to 1.
4. **Estimation of geometric imperfections:** For each cross-sectional point cloud obtained in Step 2, the modal amplitudes of the selected GBT modes are estimated using an ICP-like iterative procedure. Starting from the undeformed cross-section midline, a set of reference nodes corresponding to the intermediate nodes of the GBT cross-section discretization is considered. At each reference node, two "surface" points are defined by offsetting the midline along the plate normal by half the thickness. It should be noted that for the C cross-section, only the outward "surface" point is used, since the interior surface of the profile could not be reliably captured by the 3D scan in the flange-lip region.

   A KD-tree nearest neighbor search is used to associate each "surface" point with its closest measured point in the corresponding cross-section point cloud. Based on these associations, a linear least-squares problem of the form

$$\min_{\boldsymbol{\phi}} \|\boldsymbol{\Xi}_U \boldsymbol{\phi} - \boldsymbol{d}\|_2^2 \tag{3}$$

   is assembled, where $\boldsymbol{\Xi}_U$ is a matrix containing the GBT deformation mode functions evaluated at the reference points, $\boldsymbol{\phi}$ is the vector of modal amplitudes to be determined, and $\boldsymbol{d}$ is the displacement vector relating the cross-section midline to the nearest neighbor points.

   The estimated modal amplitudes are then used to update the deformed cross-section midline. The plate normals are recomputed to account for the deformed geometry, and new "surface" points and nearest neighbor associations are obtained. This process is repeated iteratively until convergence is achieved, as determined by prescribed tolerances on the relative change in $\boldsymbol{\phi}$, the root-mean-square residual error, and the fraction of updated nearest neighbor associations.

   Figs. 7 and 8 show the GBT deformations modes for the cross-sections of P6 and P11 profiles, the corresponding modal amplitudes along the length of the profile (with linear interpolation assumed between consecutive cross-sections), and representative reconstructed deformed cross-sections. For the sake of clarity, only the first few deformation modes are presented.

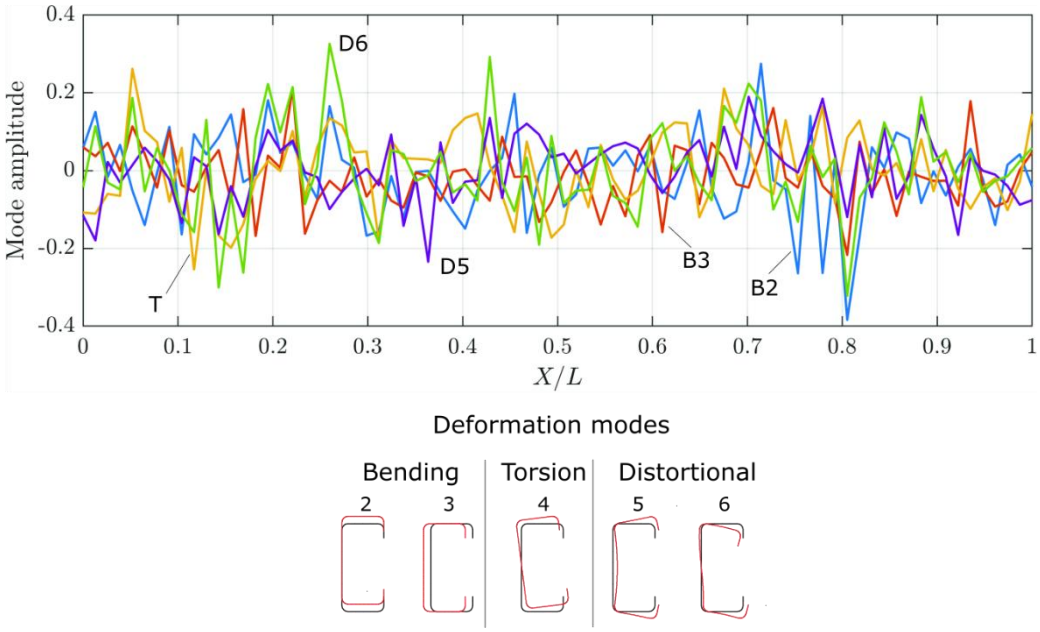

Figure 7: Profile P6: modal amplitudes and deformation modes

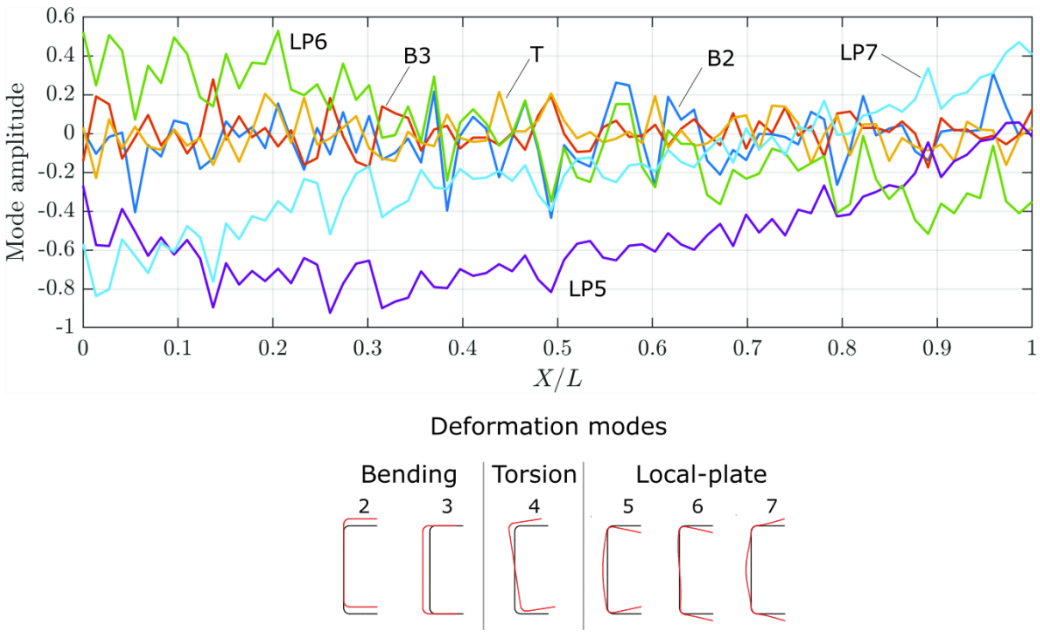

Figure 8: Profile P11: modal amplitudes and deformation modes

4.4 Test setup, procedures and instrumentation

The structural tests were also conducted at LERM-IST. Three types of instrumentation were used to acquire data from each of the 10 tested specimens: (i) a loading control system operating under displacement control in an Instron 5989 UTM with a 600 kN load capacity (identical to the one used in the material characterization tests), (ii) linear variable differential transducers (LVDTs), and (iii) a 3D (stereo) Digital Image Correlation (DIC) system, *i.e.*, a hybrid approach combining DIC with conventional instrumentation, as suggested by Meng *et al*. (2025) to maximize insight and reliability of the test results. Additionally, an external camera was employed for photographic documentation during the tests. All tests were conducted at a constant rate of 0.2 mm/min, and all the acquisition data

(UTM, DIC and LVDTs) was recorded at a sampling rate of 1 Hz. The tests were conducted until an ultimate load reduction between 20% and 30% was achieved. Fig. 9 shows an overview of test setup (Fig. 9(a)) and a detailed view of the region near to the tested specimen (Fig. 9(b)). The LVDT instrumentation was defined based on (i) the devices available at LERM at the time of testing and (ii) the numerical planning of the tests (shell-finite element-based). It should be noted that all columns exhibit very similar values for the first two bifurcation loads, differing only in the number of local half-waves (consecutive even or odd numbers). LVDT-6 was intended to capture the half-wave with the largest amplitude when the columns exhibit an even number of local half-waves. Fig. 10 shows a schematic representation of the LVDT instrumentation employed in columns (i) P1-P3 (Fig. 10(a)), (ii) P4-P6 (Fig. 10(b)), and (iii) P8-P11 (Fig. 10(c)). A negative displacement corresponds always to a reduction in the LVDT stroke and the notation for the displacement of LVDT-X is denoted by $d_{\text{LVDT-X}}$ (X: 1, 2,…,6).

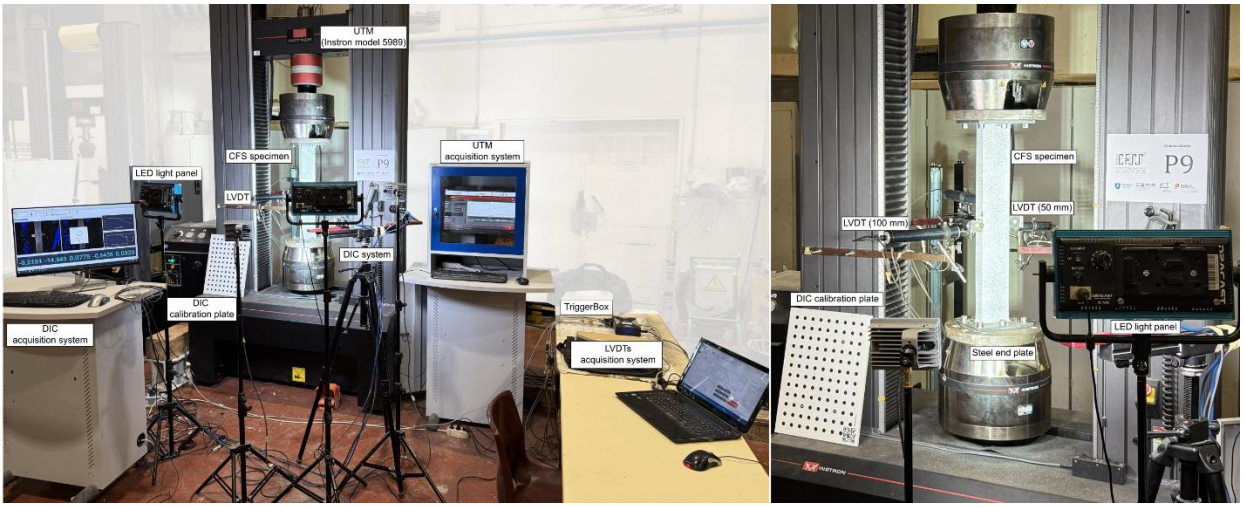

(a) (b)

Figure 9: Compression test setup (a) complete view, and (b) detailed view of setup of columns P9-P11.

4.5 Results and discussion

4.5.1 U-sections

Fig. 11 shows the equilibrium paths of the 4 U-columns tested, namely: (i) the ratio between the applied load (P) and the numerical critical local buckling load (P_{crL}), plotted against the UTM crosshead displacement (P/P_{crL} vs. $d_{\text{crosshead}}$ – Fig. 11(a)), and (ii) the same load ratio plotted against the displacement measured by LVDT-3 (P/P_{crL} vs. $d_{\text{LVDT-3}}$ – Fig. 11 (b)). The experimental ultimate loads ($P_{\text{U,Exp}}$) attained by the U-columns are reported in Table 6, while the corresponding collapse modes are illustrated in Fig. 12. As expected, all columns exhibited a typical local buckling failure mode and high post-critical strength, given the high local slenderness values (λ_{L} close or higher than 2.0, see Table 6): the values of $P_{\text{U,Exp}}/P_{\text{crL}}$ are 1.72 (P8), 1.77 (P9), 1.89 (P10) and 1.91 (P11), and a noticeable increase in this load ratio is observed as the h/b ratio increases. The collapse modes of the U-columns exhibit 5 local half-waves, identical to the critical local buckling mode, and display either *outward* ($d_{\text{LVDT-1}}<0$ and $d_{\text{LVDT-5}}<0$) (column P8) or *inward* ($d_{\text{LVDT-1}}>0$ and $d_{\text{LVDT-5}}>0$) (columns P9, P10, and P11) mid-height web-flange motions. Moreover, the experimental critical buckling loads ($P_{\text{crL,Exp}}$), determined using the so-called $P–W^2$ method (Singer *et al*. 1998), where W denotes the maximum deflection, measured from the LVDT-3 readings, are also reported in Table 6 together with the corresponding numerical values. A comparison between the experimental and numerical critical buckling loads reveals a strong agreement, with differences not exceeding 3.9 %.

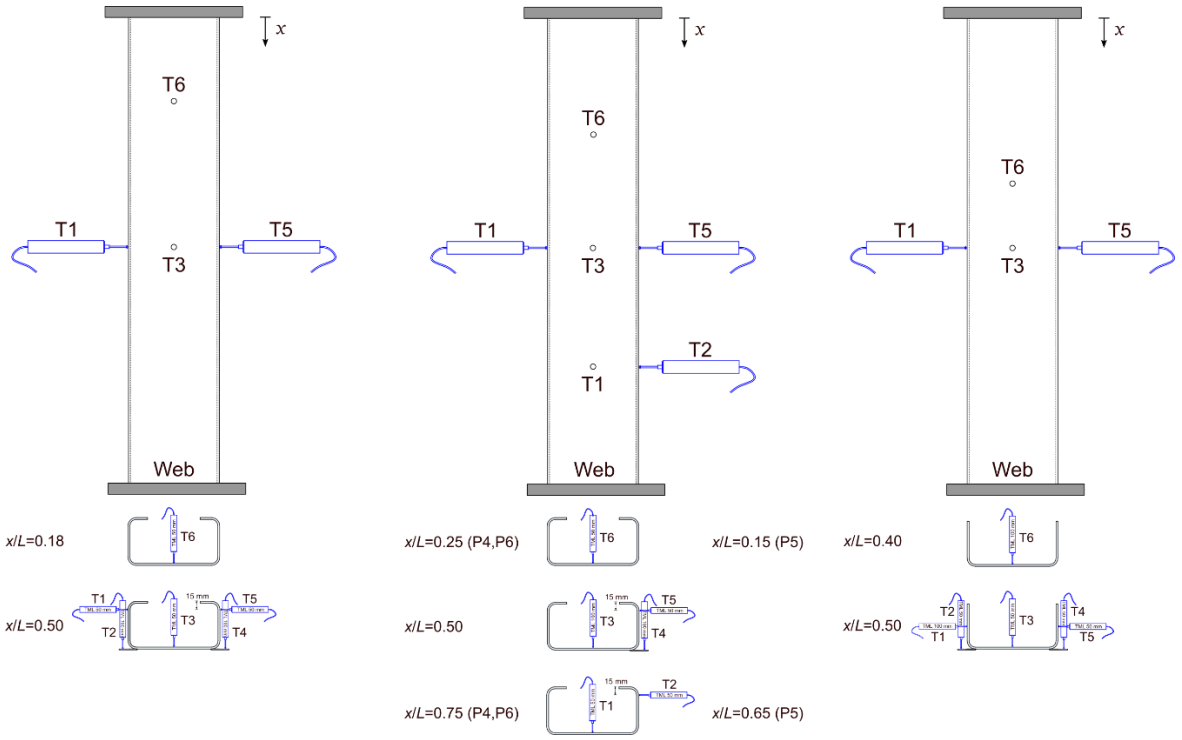

Figure 10: Location of the LVDTs at top and mid-height cross-sections for the (a) P1, P2 and P3, (b) P4, P5 and P6, and (c) P8, P9, P10 and P11.

Since the qualitative behavior of the four U-shaped columns is similar, the behavior of column P11 is selected to be presented in more detail. Fig. 13 compares the displacement readings obtained from LVDT-3 ($w_{\text{mid-web}}$) with the results provided by DIC, together with selected photographs of column P11 deformed configurations along the loading procedure. Fig. 14 illustrates the evolution of the same displacement along the loading path, accompanied by several out-of-plane displacement field (w) colormaps corresponding to (i) 8 equilibrium points (Fig. 14(a), using an identical scale for w) or (ii) 9 equilibrium points (Fig. 14(b), using independent scales for w). It should be noted that the region of interest (RoI) of the DIC does not cover the entire column length, as a small portion near the top of the

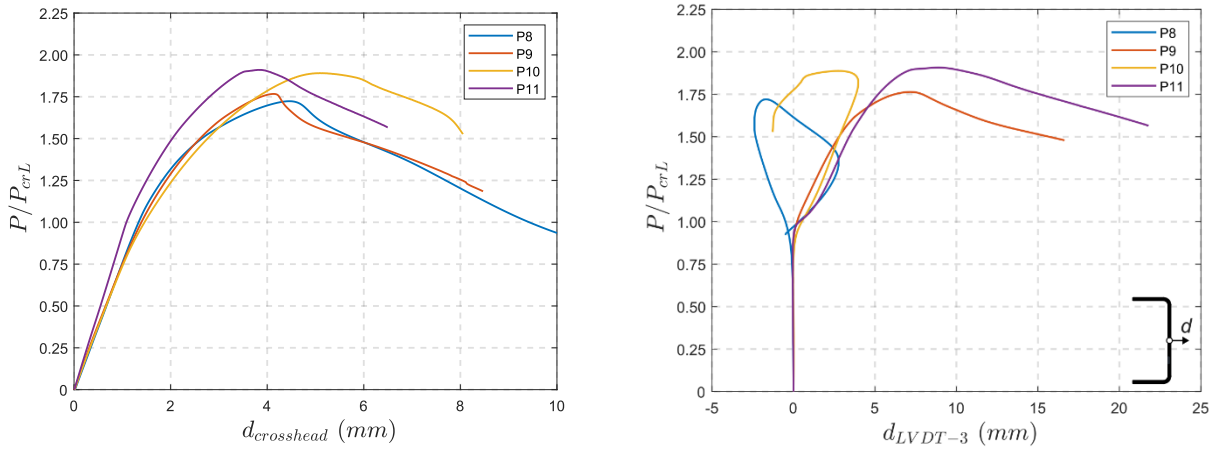

Figure 11: Equilibrium path of U-columns: (a) P/P_{crL} vs. $d_{\text{crosshead}}$ and (b) P/P_{crL} vs. $d_{\text{LVDT-3}}$.

(a) (b) (c) (d)

Figure 12: U-columns deformed configurations at the maximum load for: (a) P8, (b) P9, (c) P10 and (d) P11.

column was not captured by the cameras – a total of 585 mm (out of 750 mm) is displayed. Lastly, Fig. 15 presents transverse displacement profiles associated with the equilibrium points "A" to "I", identified in Fig. 14. A detailed analysis of this set of results leads to the following observations/remarks:

(i) First of all, there is an excellent agreement between the results obtained from conventional instrumentation and those obtained using DIC.

(ii) The column exhibits a linear-elastic response up to the vicinity of P_{crL}, as is shown in Fig. 11(a), followed by a smooth nonlinear transition until the collapse load is reached, and subsequently by a pronounced descending branch.

(iii) Fig. 14 shows the formation of 5 local half-waves from $P/P_{crL}\approx 1.0$ (point "C") up to point "D", where the local half-waves are already clearly visible (*e.g.*, Fig. 11(b)). Subsequently, as loading progresses, two less pronounced half-waves develop near the column ends, as observed at points "E" and "F" in Fig. 14 and in the corresponding transverse displacement profiles shown in Fig. 15(a). At this stage of loading, a pronounced contribution from minor-axis flexure deformation is already present, arising from the stress distribution induced by the local deformation – see the transverse displacement profiles in Fig. 15(b). This well-known effect is due to a shift in the centroid,

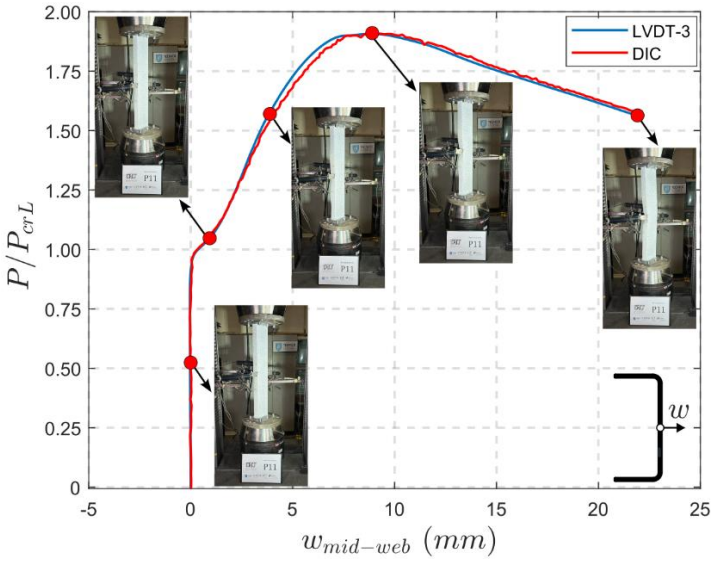

Figure 13: P/P_{crL} vs. $w_{mid\text{-}web}$ equilibrium path of column P11: LVDT vs DIC results.

which causes minor-axis bending moment inducing compression in the flanges (see *e.g.*, Young & Rasmussen 1998). This effect rapidly erodes the column strength, leading to the formation of a plastic hinge in the mid-height region (*e.g.*, see the deformed configuration of the column at the onset of the end of the testing procedure in Fig. 13). Consequently, the central local half-waves become less pronounced in the mid-height region (*e.g.*, see colormaps corresponding to points "G" to "I").

(iv) Lastly, it is observed that the column deformation is not symmetric with respect to mid-height (*e.g.*, see colormaps corresponding to points "G" to "I" in Figs. 14(a)+(b)), most likely due to some load application eccentricity and/or an irregular pattern of initial geometric imperfections.

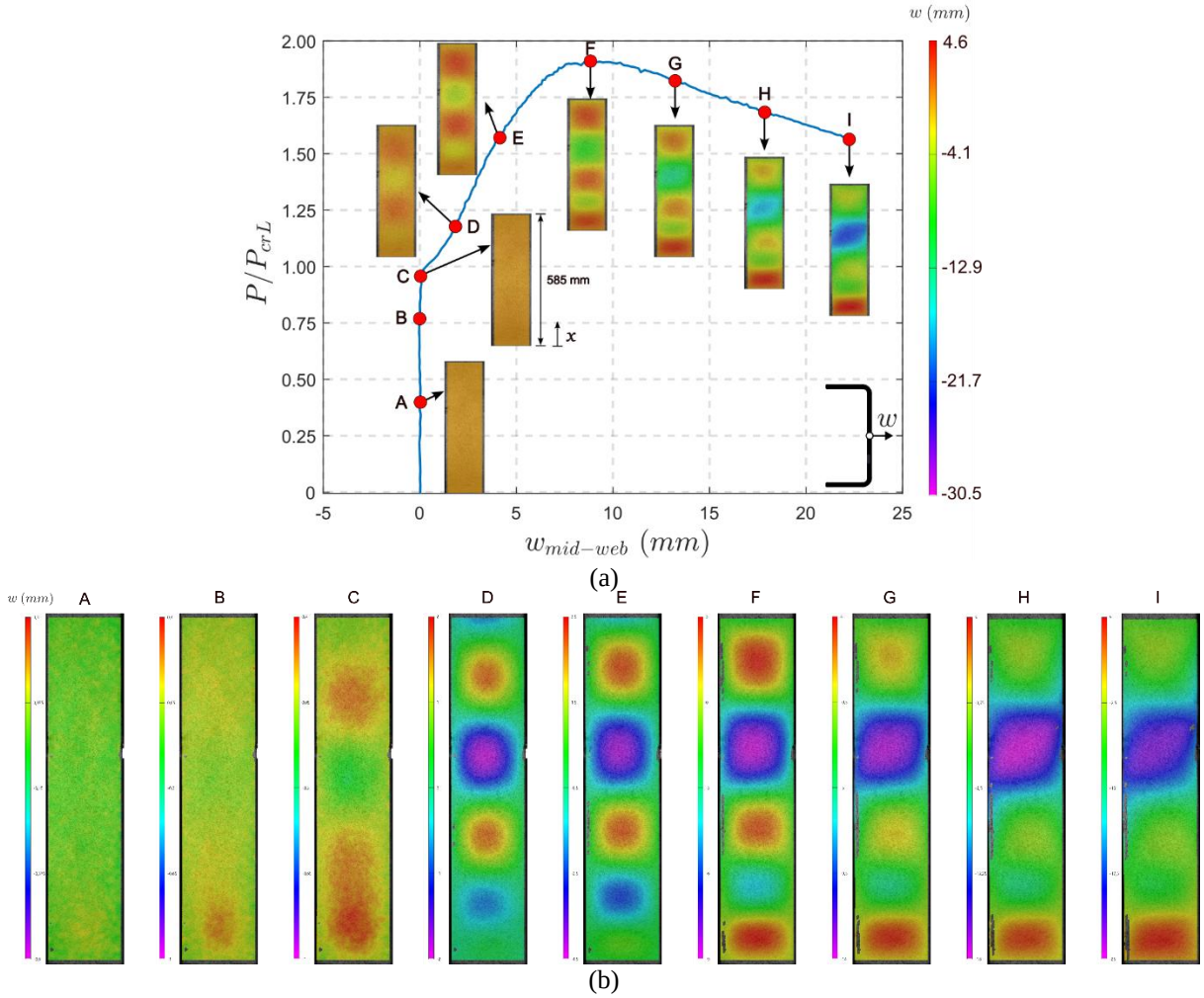

(a)

(b)

Figure 14: (a) P/P_{crL} vs. $w_{mid\text{-}web}$ equilibrium path of column P11, and (b) with selected DIC-based out-of-plane displacement colormaps.

4.5.2 C-sections

Similarly to Fig. 11 for U-columns, Fig 16 shows the equilibrium paths of the 6 tested C-columns: P/P_{crL} vs. $d_{crosshead}$ (Fig. 16(a)) and P/P_{crL} vs. $d_{LVDT\text{-}3}$ (or $d_{DIC\text{-}3}$, discussed ahead, Fig. 16(b)). The exception concerns column P3, for which LVDT-3 malfunctioned and did not allow displacement measurements during the initial loading stage, therefore, the DIC results were used instead. The experimental ultimate loads attained by the C-columns are reported in Table 6, while the corresponding collapse modes are

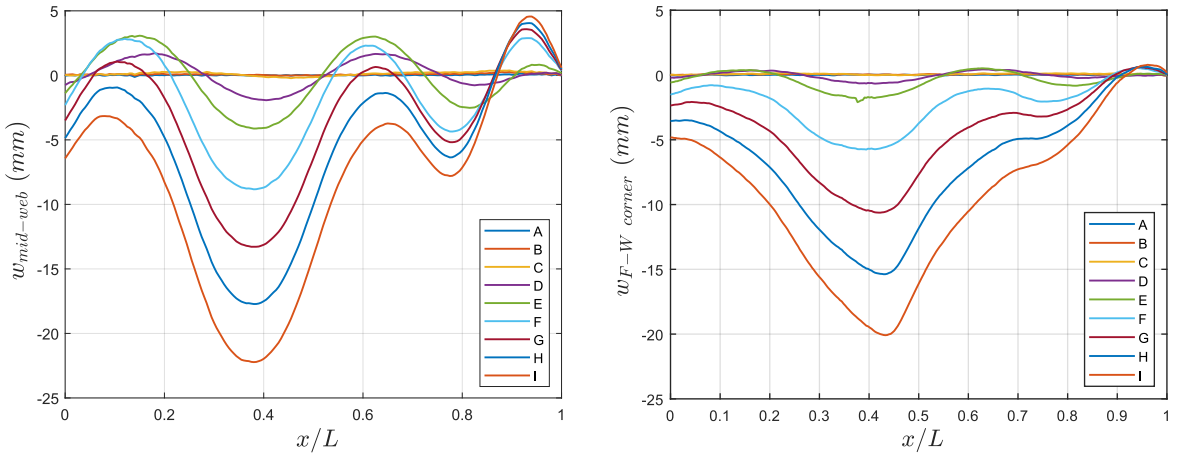

(a) (b)

Figure 15: Transverse displacement profiles of equilibrium points "A" to "I" indicated in Fig. 14: (a) mid-web and (b) left web-flange corner (L is the portion of the captured length by the cameras: 585 mm).

illustrated in Fig. 17. The results indicate that columns P1 to P5 failed by local buckling, while column P6 displayed a L-D interactive failure. Varying degrees of post-critical strength are observed: $P_{U,Exp}/P_{crL}$ = 1.72-1.61-1.32-1.27-1.75-1.69 for columns P1-P2-P3-P4-P5-P6, respectively. The analysis of the DIC-based out-of-plane displacement profiles in the web at the onset of collapse showed that columns P1-P2-P3-P5, P4, and P6 exhibited 5, 10 and 8 local half-waves, respectively, identical to the corresponding n_L values (Table 6). The $P_{crL,Exp}$ values were also determined using the P–W^2 method and are also reported in Table 6, together with the corresponding numerical values. With the exception of column P6, the maximum deflection W was obtained from the LVDT-3 measurements. Column P6 exhibited an even number of half-waves, hence the maximum deflection did not occur at mid-height and DIC-based results were used instead to determine W (*i.e.*, using the nearest local half-wave at mid-height). Once again, a good agreement between the $P_{crL,Exp}$ and P_{crL} was found, with differences below 6.6 %.

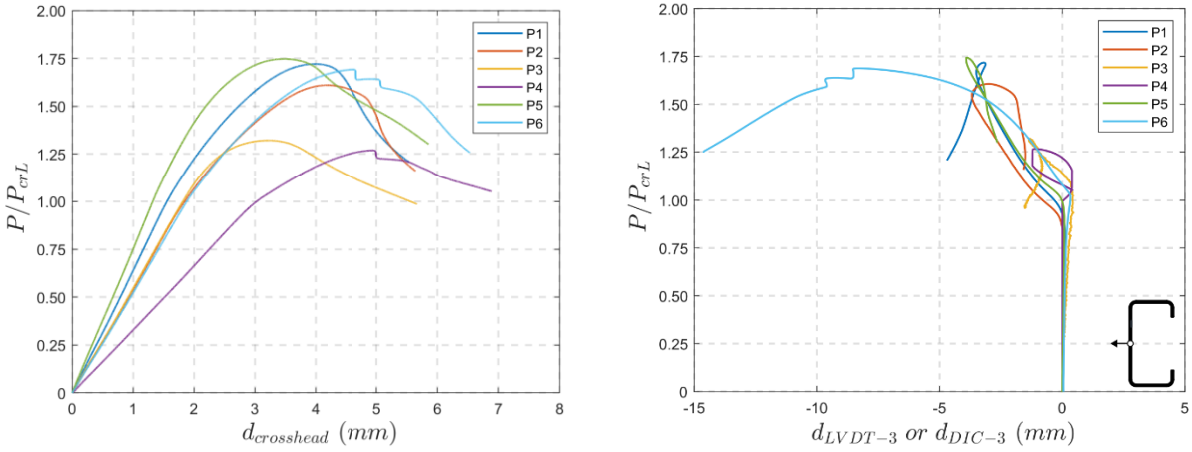

(a) (b)

Figure 16: Equilibrium path of C-columns: (a) P/P_{crL} vs. $d_{crosshead}$ and (b) P/P_{crL} vs. d_{LVDT-3} (or d_{DIC-3}).

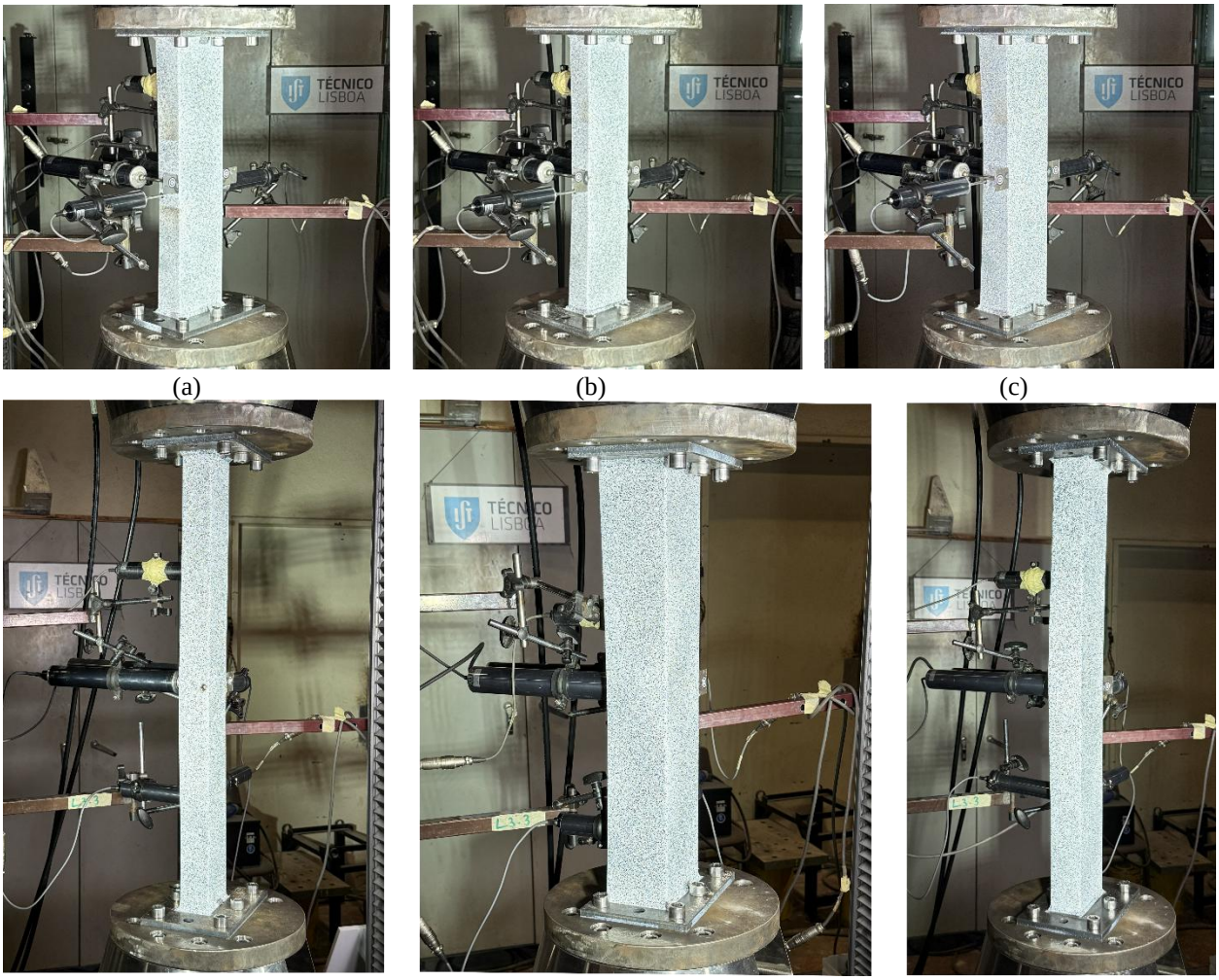

(a) (b) (c)

(d) (e) (f)

Figure 17: C-columns deformed configurations at the maximum load for (a) P1, (b) P2, (c) P3, (d) P4, (e) P5 and (f) P6.

Since the behavior of columns P1 to P5 does not differ markedly from that discussed in the previous section, as they all exhibit typical local post-buckling behavior, only the structural response of column P6 is presented in detail. To validate the DIC-based results, Fig. 18 compares the displacement measurements obtained from LVDT-3 ($w_{\text{mid-web}}$) with those provided by DIC, together with 6 selected photographs of column P6 taken at different stages of loading. Fig. 19 illustrates the evolution of the same displacement along the loading path, together with several out-of-plane displacement (w) colormaps corresponding to 9 equilibrium points. The colormaps are presented either using an identical w scale (Fig. 19(a)) or using independent w scales (Fig. 19(b)). As in the previous case (column P11, Section 4.5.2), the DIC RoI focused the central portion of the column (approximately 515 mm). Finally, Fig. 20 presents transverse displacement profiles associated with points "A" to "I" identified along the equilibrium path displayed in Fig. 19. The observation of all these results leads to the following comments:

(i) An excellent agreement is observed between the results obtained from conventional instrumentation and those derived from DIC (Fig. 18).

(ii) The column initially exhibits linear-elastic behavior up to approximately $0.6P_{\text{crL}}$. At $P/P_{\text{crL}}\approx1.0$, a w-sign reversal occurs at mid-web, followed by a pronounced strength increase up to $P/P_{\text{crL}}\approx1.50$

– note that this column exhibited an even number of half-waves. As shown in Fig. 18, for P/P_{crL}>1.50, a marked decrease in the slope of the equilibrium path (i.e., stiffness degradation) is observed until the ultimate load is finally reached at P/P_{crL}=1.69. Subsequently, the response follows a pronounced descending path.

(iii) The web displacement field *w* corresponding to point "B" ($P/P_{crL}\approx1.0$) shows that 5 (out of 6) half-waves are already visible in the central segment, exhibiting unequal amplitudes, with the largest amplitudes occurring near the lower segment. As loading continues until $P/P_{crL}\approx1.5$, the 6 local half-waves become progressively more pronounced, as observed in the displacement fields corresponding to points "C", "D", and "E", as well as in the associated transverse displacement profiles shown in Fig. 20(a). Up to this loading stage, the column exhibits a typical local post-buckling behavior.

(iv) For higher load levels (P/P_{crL}>1.5), a distortional half-wave starts to emerge, exhibiting outward flange-lip motions (*e.g.*, equilibrium point "E"). The emergence, at fairly advanced loading stages of distortional deformation akin to the critical distortional buckling mode, marks the onset of "secondary-distortional bifurcation" L-D interaction (Martins *et al*. 2015, 2018). As the load increases toward the ultimate value, this distortional half-wave grows significantly (equilibrium point "F"), as illustrated in more detail by the photographs presented in Fig. 21 (a)+(b). Consequently, these distortional deformations change significantly the shape of the transverse displacements as shown in Fig. 20(a). Once distortional buckling is triggered, the distortional deformations grow rapidly and outweigh their local (and minor-axis flexural) counterparts, which is a characteristic of the L-D coupling phenomenon (Martins *et al*. 2018).

(v) The transverse displacement profiles shown in Fig. 20(b) show the contribution from (i) (mostly) minor-axis flexure, arising from the stress distribution, and (ii) local and distortional deformations since they are not exactly plotted at the corners.

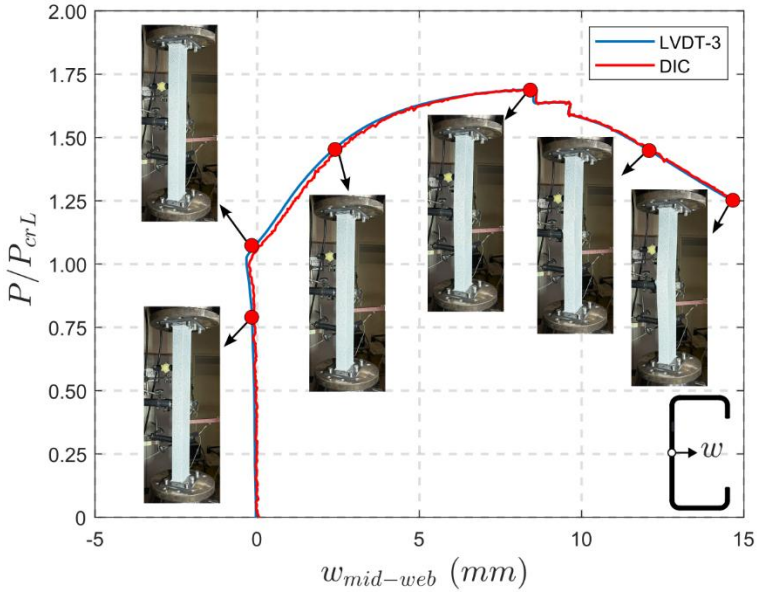

Figure 18: P/P_{crL} vs. $w_{mid\text{-}web}$ equilibrium path of column P6: LVDT vs DIC results.

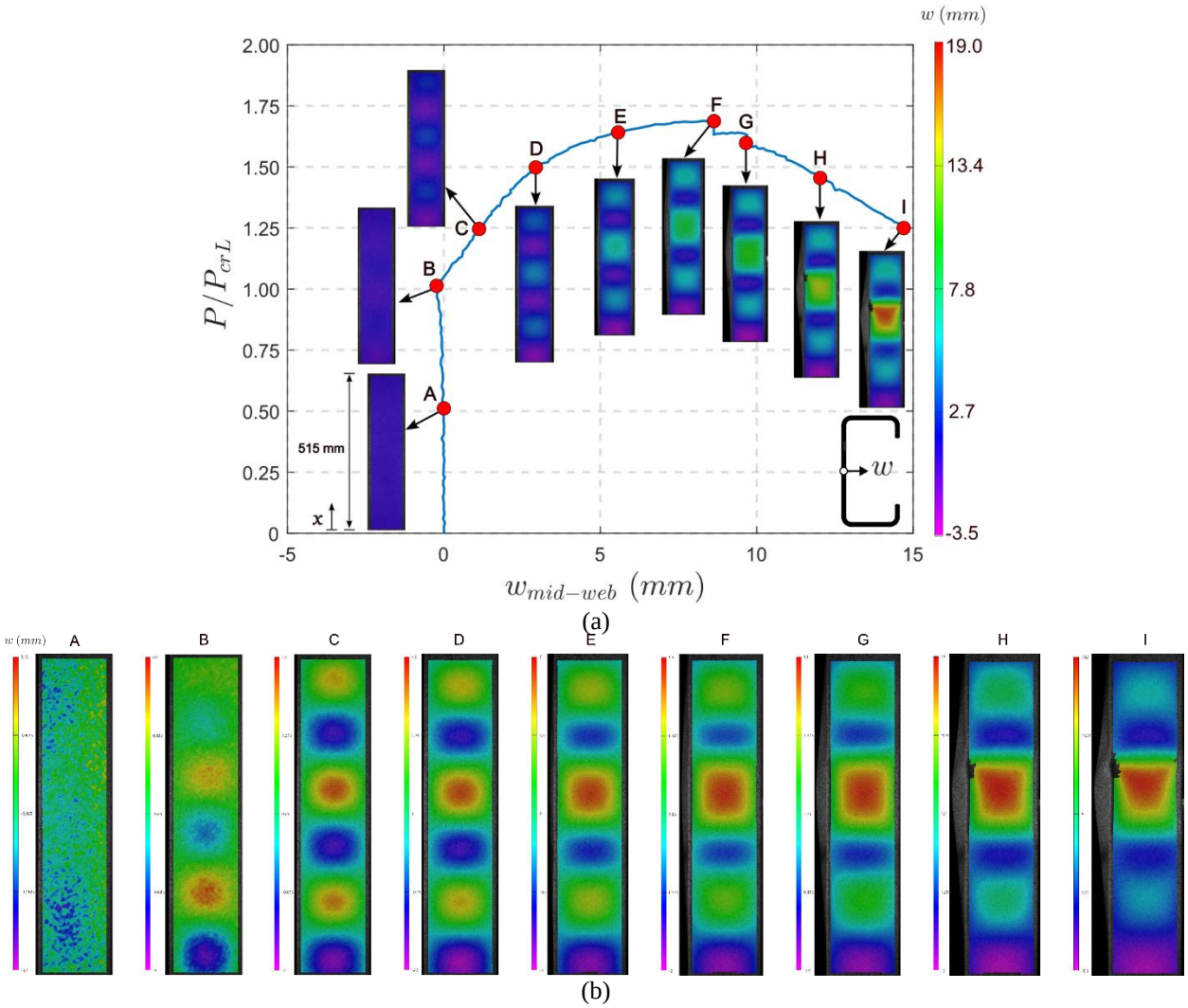

Figure 19: (a) P/P_{crL} vs. $w_{mid\text{-}web}$ equilibrium path of column P6, and (b) with selected DIC-based out-of-plane displacement colormaps.

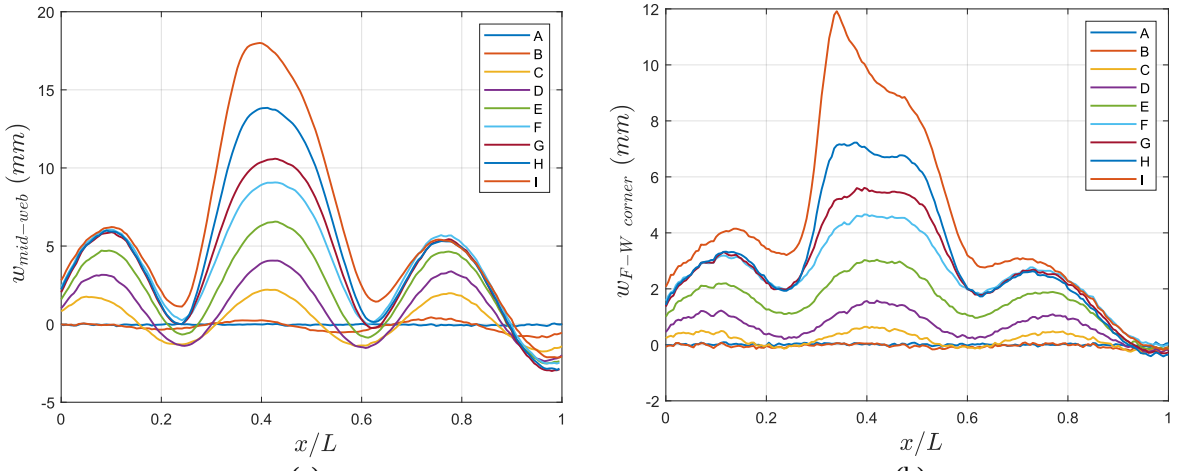

Figure 20: Transverse displacement profiles of equilibrium points "A" to "I" indicated in Fig. 19: (a) mid-web and (b) right web-flange corner (L is the portion of the captured length by the cameras: 515 mm).

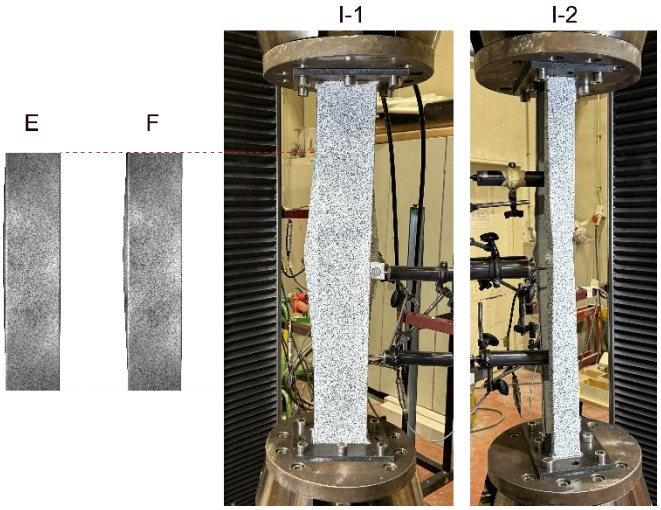

Figure 21: P6 column deformed configurations at equilibrium states "E", "F" and "I" (2 views) indicated on the equilibrium path displayed in Fig. 19(a).

5. Conclusions

This work reported an experimental investigation on the structural behavior of high-strength cold-formed steel (CFS) columns with to short and short-to-intermediate lengths, carried out at the University of Lisbon – the Phase I of a two-phase experimental campaign conducted within the scope of the NXGEN-CFSS research project: "Towards the Next Generation of Cold-Formed Steel Structures: Advanced High Strength Steels". The experimental programme began with 93 tensile tests conducted to characterize the material and assess its variability, using high-strength steel sheets of grade S700 (Strenx® 700 CR). Subsequently, sheets of the same material were press-braked to produce 4 U-shaped and 6 C-shaped cross-section profiles for structural testing. Prior to the structural tests, the 10 CFS profiles were scanned using a high-resolution handheld 3D laser scanner to determine the initial geometric imperfections. The structural tests were performed under displacement-control at a constant rate of 0.2mm/min with two complementary data acquisition systems: (i) Linear Variable Differential Transformers (LVDTs), and (ii) a Digital Image Correlation (DIC) system, which were used to measure displacements and strains throughout the structural response. The discussion of the structural results included (i) non-linear load-displacement equilibrium paths, (ii) photos showing deformed configurations along those paths (including the failure modes), (iii) DIC-based displacement fields (colormaps), (iv) transverse displacements, and (v) failure modes and loads. The most relevant conclusions drawn from this work are summarized as follows:

(i) The material characterization tests showed that (i_1) the elastic modulus (E), tensile strength (σ_u) and 0.2% proof stress ($\sigma_{0.2p}$) exhibited low variability (CoV≤5 %), while (i_2) Poisson's ratio (ν), total extension at maximum force (A_{gt}) and at fracture (A_t) exhibit slightly higher dispersion, though generally below 10%.

(ii) The constitutive model proposed by Xia *et al*. (2021), consisting an enhanced two-stage Ramberg-Osgood model, showed excellent agreement with the experimental results and is therefore deemed appropriate for modelling the Strenx® 700 CR steel.

(iii) The Lognormal and Gamma distributions were found to be suitable for modelling E, σ_u, $\sigma_{0.2p}$, ν, A_{gt}, and A_t, regardless of the goodness-of-fit test considered (Chi-square or Anderson-Darling). This provides key data for structural reliability and/or reliability-based code calibration procedures.

(iv) Excellent agreement was observed between the results obtained from conventional instrumentation (LVDT's) and those derived from Digital Image Correlation (DIC).

(v) A comparison between the experimental (P–W^2 method, Singer *et al*. 1998) and numerical critical buckling loads also showed a good agreement, with differences below 7.0 %.

(vi) As expected, the U-profiles exhibited typical local post-buckling behaviors, with high post-critical strength that increased proportionally with the web-to-flange ratio (h/b). All U-columns exhibited 5 local half-waves at collapse, consistent with the (theoretical) critical buckling mode, both of which were captured (and quantified) using the DIC-based out-of-plane displacement fields (colormaps). Minor-axis flexural displacements, stemming from the well-known stress redistribution at advanced local-post buckling stages, were also observed and quantified.

(vii) Most of the C-columns (P1 to P5) exhibited typical local failure modes with a number of half-waves identical to that of the corresponding local critical buckling mode. The only exception was column P6, which, although initially exhibiting a local critical buckling mode, began to develop distortional deformations at $P/P_{crL} \approx 1.50$ that rapidly progressed up to the ultimate load. Column P6 ultimately failed due to a "secondary-distortional bifurcation" L-D interaction (Martins *et al*., 2015, 2018), a consequence of its high strength and the proximity of the distortional critical buckling load.

Lastly, it is worth mentioning that another experimental structural campaign is planned to gather ultimate failure data for high-strength steel columns prone to other relevant ultimate (buckling) limit states, such as distortional, global, and D-G and L-D-G interaction.

Acknowledgments

This research was funded in whole or in part by the Fundação para a Ciência e a Tecnologia, I.P. (FCT, https://ror.org/00snfqn58) under Grant UID/6438/2025 (https://doi.org/10.54499/UID/06438/2025) of the research unit CERIS. The authors also acknowledge FCT for the financial support through project NXGEN-CFSS ("Towards the Next Generation of Cold-Formed Steel Structures: Advanced High Strength Steels", 2023.13431.PEX[5]) and the individual supports through (i) CEECIND-6th edition (1st author: 2023.07694.CEECIND/CP2830/CT002011) [6] and (ii) PhD scholarship (2nd author: SFRH/BD/04925/2021)[7]. The authors also would like to acknowledge the assistance of laboratory technician Fernando Alves. For the purpose of Open Access, the author has applied a CC-BY public copyright license to any Author's Accepted Manuscript (AAM) version arising from this submission.

References

AISI-S100-16 w/S3-22 (2022). *North American Specification (NAS) for the Design of Cold-Formed Steel Structural Members*, American Iron and Steel Institute, Washington (DC).

AS/NZS 4600 (2018). *Cold-Formed Steel Structures*, 3rd Ed., Standards of Australia and Standards of New Zealand, Sydney-Wellington.

ASTM E8/E8M-16 (2016). *Standard Test Methods for Tension Testing of Metallic Materials*, American Society for Testing and Materials, West Conshohocken, Pennsylvania, USA.

Akchurin, D., Shahabeddin, T., Schafer, B. (2025). "High-strength cold-formed steel stiffened channel section: axial compressive strength and initial geometric imperfections", *Thin-Walled Structures*, Vol. 206, Part B, 112604.

[5] https://doi.org/10.54499/2023.13431.PEX

[6] https://doi.org/10.54499/2023.07694.CEECIND/CP2830/CT0020

[7] https://doi.org/10.54499/2021.04925.BD

Bebiano R., Camotim D., Gonçalves R. (2018). "GBTUL 2.0 − A second-generation code for the GBT-based buckling and vibration analysis of thin-walled members", *Thin-Walled Structures*, 124, pp. 235 - 257.

Blender Foundation (2026). *Blender* (Version 5.0), Amsterdam.

Camotim, D., Martins, A.D., Dinis, P.B., Young, B., Chen, M.-T., Landesmann, A. (2020a). "Mode interaction in cold-formed steel members: state-of-art report. Part 1: Fundamentals and local-distortional coupling", *Steel Construction: Design and Research*, Vol. 13(3), 165-185.

Camotim, D., Martins, A.D., Dinis, P.B., Young, B., Chen, M.-T., Landesmann, A. (2020b). "Mode interaction in cold-formed steel members: state-of-art report. Part 2: Couplings involving global buckling", *Steel Construction: Design and Research*, Vol. 13(3), 186-207.

Cignoni, P., Callieri, M., Corsini, M., Dellepiane, M., Ganovelli, F., Ranzuglia, G. (2008). "Meshlab: an Open-Source Mesh Processing Tool", *Sixth Eurographics Italian Chapter Conference*, pp. 129-136.

Ding, C. (2022). *Strength and Behavior of Advanced High Strength Steel Structural Components*, PhD Thesis in Civil Engineering, Johns Hopkins University, Baltimore, Maryland (USA).

Ding, C., Xia, Y., Akchurin, D., Blum, H., Li, Z., Schafer, B.W. (2022). "Structural behavior of advanced strength steel: ductility, connections, members", *Proceedings of the Cold-Formed Steel Research Consortium Colloquium*, 17-19 October (Online).

Ding, C., Xia, Y., Akchurin, D., Blum, H., Li, Z., Schafer, B.W. (2026). "Flexural strength of advanced high strength steel lipped channels", *Thin-Walled Structures*, Vol. 218 (Part C, January), 114112.

EN ISO 6892-1 (2019). *Metallic materials – tensile testing – Part 1: Method of test at room temperature*, International Organization for Standardization (ISO), Geneva, Switzerland.

EN 1990 (2023). *Eurocode 0: Basis of Structural Design*. European Committee for Standardisation (CEN), Brussels, Belgium.

EN 1993-1-3 (2024). *Eurocode 3 – Design of Steel Structures – Part 1-3: Cold-formed Members and Sheeting*, European Committee for Standardization (CEN), Brussels.

Gardner, L., Yun, X. (2018). "Description of stress-strain curves for cold-formed steels", *Construction and Building Materials*, Vol. 189 (20 November), 527-538.

Gonçalves, R., Camotim, D. (2016). "GBT deformation modes for curved thin-walled cross-sections based on a mid-line polygonal approximation", *Thin-Walled Structures*, 103, pp. 231-243.

JCSS (2001). The Joint Committee of Structural Safety (JCSS) probabilistic model code. Part III: Resistance models.

Ma, C., Su, A., Jiang, K., Zhao, O., Gardner, L. (2026). "Local buckling of S700 high strength cold-formed steel built-up I-sections subjected to combined compression and minor-axis bending", *Thin-Walled Structures*, Vol. 219(Part A, February), 114166.

Martins, A.D., Dinis, P.B., Camotim, D., Providência, P. (2015). "On the relevance of local-distortional interaction effects in the behaviour and design of cold-formed steel columns", *Computers & Structures*, Vol. 160(November), 57-89.

Martins, A.D., Camotim, D., Dinis, P.B. (2017). "Local-distortional interaction in cold-formed steel beams: behaviour, strength and DSM design", *Thin-Walled Structures*, 119(October), 879-901.

Martins, A.D., Camotim, D., Gonçalves, R., Dinis, P.B. (2018). "On the mechanics of local-distortional interaction in thin-walled lipped channel columns", *Thin-Walled Structures*, Vol. 125(April), 187-202.

Meng, X., Pullen, A., Guo, X., Yun, X., Gardner, L. (2025). "3D laser scanning and DIC structural testing: state-of-the-art, best practice and effective use", *Engineering Structures*, Vol. 345 (Part A, 15 December), 121055.

Mirambell, E., Real, E. (2000). "On the calculation of deflections in structural stainless steel beams: an experimental and numerical investigation", *Journal of Constructional Steel Research*, Vol. 54(1), 109-133.

Singer, J., Arbocz, J., Weller, T. (1998). *Buckling Experiments: Experimental Methods in Buckling of Thin-Walled Structures: Basic Concepts, Columns, Beams and Plates – Volume 1*., John Wiley & Sons, Inc.

Wang, X.-Q., Tao, Z., Katwal, U., Hou, C. (2021). "Tensile stress-strain models for high strength steels", *Journal of Constructional Steel Research*, Vol. 186(November), 106879.

Xia, Y., Ding, C., Li, Z., Schafer, B.W., Blum, H.B. (2021). "Numerical modelling of stress-strain relationships for advanced high strength steels", *Journal of Constructional Steel Research*, Vol. 182(July), 106687.

Young, B., Rasmussen, K.J.R. (1999). "Shift of effective centroid in channel columns", *Journal of Structural Engineering* (ASCE), 125 (5) 524–531.